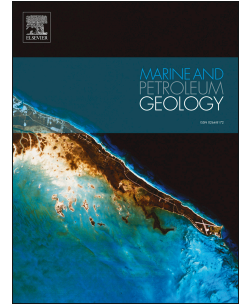


Accepted Manuscript

Gas venting that bypasses the feather edge of marine hydrate, offshore Mauritania

Ang Li, Richard J. Davies, Simon Mathias, Jinxiu Yang, Richard Hobbs, Miles Wilson



PII: S0264-8172(17)30335-5

DOI: [10.1016/j.marpetgeo.2017.08.026](https://doi.org/10.1016/j.marpetgeo.2017.08.026)

Reference: JMPG 3043

To appear in: *Marine and Petroleum Geology*

Received Date: 14 January 2017

Revised Date: 17 May 2017

Accepted Date: 22 August 2017

Please cite this article as: Li, A., Davies, R.J., Mathias, S., Yang, J., Hobbs, R., Wilson, M., Gas venting that bypasses the feather edge of marine hydrate, offshore Mauritania, *Marine and Petroleum Geology* (2017), doi: 10.1016/j.marpetgeo.2017.08.026.

This is a PDF file of an unedited manuscript that has been accepted for publication. As a service to our customers we are providing this early version of the manuscript. The manuscript will undergo copyediting, typesetting, and review of the resulting proof before it is published in its final form. Please note that during the production process errors may be discovered which could affect the content, and all legal disclaimers that apply to the journal pertain.

Gas venting that bypasses the feather edge of marine hydrate, offshore Mauritania

Ang Li ^{a*}, Richard J. Davies ^b, Simon Mathias ^a, Jinxiu Yang ^c, Richard Hobbs ^a, Miles Wilson ^a

^a Centre for Research into Earth Energy Systems (CeREES), Department of Earth Sciences, Science Labs, Durham University, DH1 3LE, UK

^b School of Civil Engineering and Geosciences, Newcastle University, Newcastle upon Tyne, Tyne and Wear, NE1 7RU, UK

^c Research Institute of Unconventional Petroleum and New Energy, China University of Petroleum, Qingdao, Shandong, 266580, China

Abstract: Methane can be released from the vast marine hydrate reservoirs that surround continents into oceans and perhaps the atmosphere. But how these pathways work within the global carbon cycle now and during a warmer world is only partially understood. Here we use 3-D seismic data to identify what we interpret to be a gas venting system that bypasses the hydrate stability zone (HSZ) offshore of Mauritania. This venting is manifested by the presence of the acoustic wipe-out (AWO) across a densely faulted succession above a salt diapir and a set of morphological features including a substantial, ~260 m wide and ~32 m deep, pockmark at the seabed. The base of the HSZ is marked by a bottom simulating reflector (BSR) which deflects upwards above the diapir, rather than mimicking the seabed. We use a numerical modelling to show that this deflection is caused by the underlying salt diapir. It creates a trapping geometry for gas sealed by hydrate-clogged sediment. After entering the HSZ, some methane accumulated as hydrate in the levees of a buried canyon. Venting in this locality probably reduces the flux of gas to the landward limit of feather edge of hydrate, reducing the volume of gas that would be susceptible for release during a warmer world.

Key words: gas hydrate, BSR, gas venting, diapir

1 Introduction

Methane is a potent greenhouse gas and vast quantities of it are stored in marine hydrate, a crystalline lattice of water and methane-dominated gas (Sloan and Koh, 2008). Its susceptibility to ambient conditions (pressure, temperature and salinity) makes it an unstable large carbon capacitor (Dickens, 2003; Ruppel, 2011). Long-term atmospheric temperatures could change if a small proportion of released gas entered the atmosphere (Archer et al., 2009). Therefore, understanding under what circumstances methane can bypass hydrated sediment and enter the atmosphere is important for assessing the impact of deep-buried methane on climatic change. Vigorous gas plumes in which gas bubbles rise within clusters and reach sea surface before not all of these gases are dissolved and oxidised in water body (McGinnis et al., 2006). This mechanism could take place where effective venting systems operate.

The feeder system for the gas vents can be detected by seismic imaging and can take the form of gas chimneys, which are vertically aligned reflections that probably represent clusters of hydraulic fractures (Hovland and Judd, 1988; Cartwright et al., 2007). Gas-rich pore fluid can be vented at different flux rates (Roberts, 2001). As a result, the morphological feature at the seabed can be pockmarks (Moss and Cartwright, 2010), pingoes that host hydrate in the near-seabed sediment (Serié et al., 2012), and mud volcanoes produced by the outflowing mud and water (Milkov, 2000). Gas venting from these point sources constitutes an important part of the known output of gas escaping from marine sediments (Judd, 2003).

Here we use 3-D seismic dataset to image what we interpret to be a gas venting system in which gas bypasses the feather edge of marine hydrates. What is unique here is the spatial relationship between the feather edge and the gas vent. It increases gas emission and hence prevents free gas from migrating landward, thus reducing the volume of gas located in the feather edge of hydrate, that is susceptible to melting during short-term ocean warming.

2 Gas hydrate and feather edge

In deep-water settings gas hydrates can be revealed by a bottom simulating reflector (BSR) in seismic reflection data. It marks the base of the hydrate stability zone (HSZ) and is produced by an acoustic impedance contrast between sediments containing gas and hydrate (Shipley et al., 1979; MacKay et al., 1994). This base shallows landwards until it intersects the seabed and this zone is termed the feather edge, a critical site for understanding the dynamics of marine hydrate (Ruppel, 2011; Berndt et al., 2014). Here ~3.5% of the global gas hydrate inventory is trapped (Ruppel, 2011) and warming of bottom water can destabilise the near-seafloor gas hydrate, which is evidenced by the presence of gas plumes (Westbrook et al., 2009; Skarke et al., 2014) and predicted by numerical modelling (Phrampus and Hornbach, 2012; Marín-Moreno et al., 2013). The released methane can lead to ocean acidification and deoxygenation and perhaps climatic warming (Kvenvolden, 1993; Archer et al., 2009; Biastoch et al., 2011).

3 Geological setting

The sedimentary features along the Mauritanian continental slope include canyon channel systems, submarine slides and contourite moats (Krastel et al., 2006). The sedimentation rates in different locations vary considerably (Krastel et al., 2006). Core samples of up to 10 m long were recovered from GeoB 8509-2, GeoB 8520, GeoB 9624-1,

GeoB 9623-2 and GeoB 9626-1 and show that the near-seabed deposit is predominately turbidite and hemi-paleogenic sediments (Zühlsdorff et al., 2007; Henrich et al., 2008; Henrich et al., 2010). Halokinesis is evidenced by the diapiric structures in a narrow elongate zone between 16 °N and 19 °N offshore the West Africa Continent and the age of the salt is probably Early Jurassic (Rad et al., 1982). A salt diapir (located in 18°30'N, 16°50'W) has been revealed by the negative Bouguer Anomaly. The study area is to the south of the Tioulit Canyon (Fig. 1). To the north seismic features of complete feather edge have been recorded before (marked by blue box of solid line in Fig. 1a, Davies et al., 2015).

Two wells, Chinguetti-6-1 and V-1, have been drilled within the 3-D seismic survey and ~30 km north of the study area, confirming that the coastal basin of Mauritania is a potential petroleum province and the Cenomanian-Turonian mudstones are able to generate hydrocarbons (Vear, 2005). Seismic features linked to vertical gas migration include seismic chimneys (Davies and Clarke, 2010) and large-scale gravity-driven faults (Yang and Davies, 2013). The BSRs, either relict or modern ones, can be observed, which makes this site ideal to research methane recycling in marine hydrate system (Davies and Clarke, 2010; Davies et al., 2012).

4 Seismic dataset and methodology

The 3-D seismic data cover an area of ~4000 km². They have been processed by multiple suppression and post-stack time migration. The final bin spacing is 25 m × 25 m. These data are displayed in two-way-travel time (TWTT). The velocity of succession investigated here is likely to be ~1800 m/s and the dominant frequency of seismic data is ~50 Hz, which together yield a vertical resolution of ~9 m. The positive acoustic impedance is recorded as a seismic trough, which is a red-black loop in the seismic profile. A good

example of the reflection having such loop is the seabed one. The BSR is a black-red loop, consistent with a negative acoustic impedance contrast. The seismic attributes used here are root mean square (RMS) amplitude and dip magnitude. Both help identify bright spots (e.g. potential hydrocarbons) and structural features (e.g. pockmarks and faults), respectively (Brown, 2010). The time window of calculating the RMS amplitudes for each map is ± 40 ms along the surface of the peaks or the troughs of a tracked reflection.

5 Observations

5.1 Fault systems and seabed features

13 planar faults (named F1 to F13) with a NNW-SSE trend are identified on the basis of clear offsets in stratal reflections (Fig. 1c). They all have a curved, concave-up geometry in cross section (Fig. 1c, d). There are additional faults that are not so clearly imaged due to acoustic wipe-out (AWO), particularly in the area bounded by F1, F2 and F4 (Fig. 2a, b). All the faults are normal, though the throw of some of the faults is indiscernible at the seismic scale. The faults have a similar angle of dip of $\sim 50^\circ$ and together form a crestral collapse graben system (Fig. 1c, d). The lower tip points of the faults are located at the top of a salt diapir (Fig. 1d). F1, F2 and F4, which are the major faults, have a throw of < 10 ms (*c.* < 9 m) near the seabed and break surface whereas other faults tip out below the seabed (Fig. 1d). The spatial correlation between the intruding diapir and the resultant faulting pattern has been seen in other settings, for example offshore of North Carolina (Schmuck and Paull, 1993) and Angola (Serié et al., 2012).

The morphological features at the seabed include fault scarps and a set of mounds and depressions (Fig. 1b, Fig. 2). Four of them are selected for description here. Their expression at the seabed varies from sub-circular to well-rounded (Fig. 2g-j). The long axis ranges from

170 m to 410 m and the positive and negative deflections are $\sim 27 - 53$ m and ~ 32 m, respectively (Fig. 2). Their morphologies on the seismic profile are a symmetrical mound (II, IV) or a depression (III), or the asymmetrical complex with a combination of both (I) (Fig. 2). The positive relief have a comparable morphology with the Arctic ice-cored hills in Canada which are driven by growth of segregated ice or intrusion and progressive freezing of a sub-pingo water lens (Mackay, 1987).

5.2 BSR and diapir

The BSR is identified based on the characteristic features of high seismic amplitude and negative polarity over the area covered by the entire seismic dataset. In this case the BSR has a geometry of an elongate, upward deflection that is analogous to an anticline (Fig. 3a), rather than mimicking the seafloor in most cases (cf. offshore Oregon, Bangs et al., 2005). Along the intersection between the faults and the BSR we identify some examples of positive relief of $\sim 20 - 30$ m in height (Fig. 2d and f, Fig. 3a). A salt diapir is ~ 1050 ms (*c.* 945 m) below seabed and characterised by a chaotic internal seismic facies. Its top reflection is a red-black loop representing the same polarity with seabed (Fig. 2). The diapir is elongated along the NNW-SSE direction that is similar to the trend of the faults. Its hinge line is spatially coincident as the region of maximum deflection of the BSR.

The RMS amplitude map of the BSR displays some high-amplitude anomalies, most of which are within the convex upward part of the BSR (Fig. 3b). These anomalies, which we refer to as high-amplitude bands, have a crescent or linear geometry (Fig. 3b). Their strike does not coincide with the depth contour of the BSR. Their width ranges from 150 m to 500 m. For each band, the amplitude variation is symmetrical, with the highest amplitude in the middle of the band and decreasing to both of its sides (Fig. 3b).

5.3 Positive high amplitude anomaly (PHAA) in levees

There are a set of ENE-WSW oriented buried canyons which have a low sinuosity (Fig. 3 and 4) above the BSR. These canyons have a multistory, aggradational and laterally offset stacking pattern (Fig. 4a), which is similar to that of the channel-levee system in offshore Nile delta (Catterall et al., 2010). The paleo-canyons are buried 50 – 65 ms (*c.* 45 – 58.5 m) below the seabed and have a V-shaped cross-sectional morphology. The steepness of the canyon walls decreases with decreasing burial depth. Sediments filling in the canyons have sub-horizontal reflections (Fig. 4a). Three paleo-canyons are recognised and of our interest is the oldest one that has a width of ~450 m in seismic cross section (marked in blue in Fig. 4a). The depth of the channel ranges from 25 to 45 ms in TWTT (*c.* 22.5 – 40.5 m) and increases with water depth. The thalweg trend is sub-parallel to the dip of the modern seabed (Fig. 3b). It bifurcates near F1 (Fig. 4d), but the accurate location of divergence is unclear due to the overprinting effect of the BSR.

The reflections, which downlap upon the paleo-seabed B (marked in dashed orange lines of Fig. 4a), are interpreted to represent sediments deposited in levee. Some positive high amplitude anomalies (PHAAs) are found within these reflections. These PHAAs originate from the place where the BSR intersects with F1 (Fig. 4c, d). They are juxtaposed along F2 and fade out in an up-dip direction (Fig. 4d). The amplitude map of reflection A shows that the PHAAs occur at both flanks of the canyon, each with a wedge-like geometry (Fig. 4d). In plan view they are bounded by the canyon wall and F2. The maximum value of the PHAA is largest near F2 and the amplitude values decrease updip and also away from the canyon (Fig. 4d).

6 Interpretations

6.1 Gas venting

AWO is a seismic response to gas filling in pores of sediment, which causes decrease of P-wave velocity, severe ray bending, signal scattering and high transmission loss (Anderson and Hampton, 1980). The result of signal lost or scattered is presented as acoustic fade-out or wipe-out in the seismic cross section. The cores sampled as the shallow sediment in the Bering Sea confirmed that AWO is caused by gas (Abrams, 1992). Therefore, we interpret that the AWO zones, either ~200 m wide below the features of I–IV or km-scale wide ~300 m below the BSR (Fig. 2), indicate the presence of free gases and escaping of gas along faults towards the seabed.

The sub-circular depression (III, Fig. 2), which is a pockmark, suggests the occurrence of venting of gas-rich pore fluid (Cartwright and Santamarina, 2015; Hovland and Judd, 1988). The positive relief of I, II and IV could be the mud cone, the sediment of which is unloaded onto the seabed after being transported vertically in a liquefied way (Dimitrov, 2002). Their morphology is comparable to the mud volcanos found in the Gulf of Cadiz but of smaller dimension (Somoza et al., 2003). The rate of the migration related to formation of mud cones is documented to be fast (Roberts, 2001). Alternatively, the local up-bending of the seabed could solely result from hydrate accretion, during which pore volume will expand due to the less density of methane hydrate than that of seawater (Soloviev and Ginsburg; 1994). Such features, named as pingos, were seen in offshore of Angola (Serié et al., 2012) and Norwegian Sea (Hovland and Svensen, 2006), which were interpreted to suggest seepage of hydrocarbon gas. Actually when focused fluid expulsion has a varying flux, its expression at the seabed has a spectrum of features, rather than an exclusive one (Roberts, 2001; Roberts et al., 2006). In the venting system, the flux rate may vary with time and space, thus it is

likely that some features mentioned above may occur in a locale simultaneously and their seismic features could overprint on each other. Overall, the presence of these features coupled with AWO is compelling evidence of gas bypassing the feather edge of marine hydrate.

6.2 Gases trapped below the BSR

In seismic reflection data high-amplitude bands (Fig. 3d) are a common seismic response to the interface between hydrated sediments above the BSR and gas-bearing sediments below it (Davies et al., 2015). Similar features have been described before by Li et al. (2016) in the same seismic survey. Most of the bands here are within the upwarping region of the BSR (Fig. 3b). The relief in the BSR creates a trapping geometry for free gas (Kvenvolden, 1993). Furthermore, under the eastern flank of the upwarping BSR we found a set of flat spots (Fig. 3a), an evidence for the phase boundary between gas and water, or gas and oil (Brown, 2010). Therefore, we interpret that free gases are trapped below the BSR.

6.3 Hydrates hosted in levees

Silty sand can be found in the cores sampled in levee successions near the seabed (Henrich et al., 2010) and it potentially traps gas and hydrate stratigraphically. Hydrate filling in pores of sediment can increase its acoustic impedance to the level such that it can be displayed as enhanced reflections in seismic data because of a higher P-wave velocity of methane hydrate (3750 – 3800 m/s, Helgerud et al., 2009). We interpret the PHAAs (marked in Fig. 4d) as an isolated methane hydrate trap. The fact that the PHAAs have lower amplitude than the BSR coincides with the synthetic seismic result which reveals that in marine sediment gas/hydrate phase boundary normally has a higher acoustic impedance contrast than the hydrate/brine interface (Zhang et al., 2012).

The amplitude variation of the PHAAs at reflection A may be the result of gas migration. We interpret that gas breached the sealing at the level of BSR near the intersection between faults and reflection A. The juxtaposition of the high-amplitude reflections along F2 (Fig. 4c) suggests that the sediments represented by these PHAAs could be inter-connected and permeable before faulting. If this gas could migrate along the levees, Darcy's law would allow us to predict that the concentration of hydrate converted from gas decreases with distance towards up dip. This result is consistent with amplitude variation at reflection A. An alternative explanation for the amplitude variation in the PHAAs is the distribution of pores of sediment, the prediction of which can be guided by sedimentology. In a channel-levee system the coarser-grained sediment was unloaded near the channel, while the finer-grain one in distance. Given that the primary pores narrowed uniformly after compaction, the sediment near the channel can host more hydrate than that far away from channel. However, which factor controls the amplitude variation is uncertain in this case.

7 Discussion

7.1 BSR deflection

The upward deflection of the BSR has been seen before (Hornbach et al., 2005) and is attributed to the underlying salt diapir which has a higher thermal conductivity and hence changes thermal regime. Here to testify whether the salt diapir affects the BSR depth, we assume the thermal conductivity of the salt ($6 \text{ W m}^{-1} \text{ K}^{-1}$, Hornbach et al., 2005) then use the 2-D heat conduction modelling. Its steady state can be expressed as:

$$k_x \frac{\partial^2 T}{\partial x^2} + k_z \frac{\partial^2 T}{\partial z^2} = 0$$

where $T[\Theta]$ is the sediment temperature, $x[\text{L}]$ and $z[\text{L}]$ are the sediment length and depth below the seafloor, respectively. $k_x[\text{MLT}^{-3}\Theta^{-1}]$ and $k_z[\text{MLT}^{-3}\Theta^{-1}]$ is the sediment thermal conductivity in the horizontal and vertical direction, respectively. The subsurface sediment

other than that within the salt diapir is assumed to be isotropic and homogeneous. An enhanced red reflection is interpreted as the top of the salt diapir (Fig. 5) and the nodes below it are assumed to have a higher thermal conductivity than the surrounding sediments ($1 \text{ W m}^{-1} \text{ K}^{-1}$). Any middle point of two known neighbouring nodes A and B has a thermal conductivity k_{AB} :

$$k_{AB} = 2(1/k_A + 1/k_B)^{-1}$$

where $k_A[\text{MLT}^{-3}\Theta^{-1}]$ and $k_B[\text{MLT}^{-3}\Theta^{-1}]$ is the thermal conductivity at node A and B, respectively. We obtain the pressure profile by assuming the hydrostatic pressure gradient of 10.09 MPa/km . The BSR depth is determined by the intersecting point of geotherm and methane hydrate stability curve (we assume gases are 100% methane). The latter has been digitalised by Lu and Sultan (2008) and a correction of seawater salinity of 35 ppt on this stability curve is made. The 2-D steady state equation is then discretised in space using finite differences and solved using MATLAB's `MLDIVIDE` function. The model has a 350×800 cell temperature grid and is subjected to the boundary conditions:

$$\begin{aligned} T &= T_{SB} + J(z - z_{SB}), & x = 0 \text{ km}, & & z_{SB} \leq z \leq 5 \text{ km} \\ T &= T_{SB} + J(z - z_{SB}), & x = 8 \text{ km}, & & z_{SB} \leq z \leq 5 \text{ km} \\ \partial T / \partial z &= J, & 0 \text{ km} \leq x \leq 8 \text{ km}, & & z = 5 \text{ km} \\ T &= T_{SB}(z), & 0 \text{ km} \leq x \leq 8 \text{ km}, & & z = z_{SB}(x) \end{aligned}$$

where $T_{SB}[\Theta]$ is the temperature of the seabed and at each water depth, $z_{SB}(x)[\text{L}]$, the seabed temperature, $T_{SB}(z)[\Theta]$, is obtained from World Ocean Data (WOD). $J[\Theta\text{L}^{-1}]$ is the geothermal gradient. This model is first used in the places where the BSR mimics the seabed to get the geothermal gradient fitting best with the seismic observation (32°C km^{-1}), then in the study area.

The result shows that the modelled BSR has a good match with the observed one, particularly across the crest of the diapir (Fig. 5). This implies that the salt diapir changed the

thermal regime and hence controls the geometry of the BSR. This increases the vertical relief of the BSR and therefore the relief of the trap. It is likely that some of the local mismatches, in particular the ones characterised by the local positive relief that is ~100 – 300 m wide adjacent to some of the faults (marked by the right two black arrows in Fig. 5), may be caused by warm focused flow that leads to local hydrate re-equilibrium (Crutchley et al., 2014). Therefore, the BSR relocation is the result of heat transfer in the form of diffusion coupled with local advection. However, there are some uncertainties that lead to the inaccuracy of the modelling result. Ionised salt can hinder hydration, leading to the thinning of the HSZ (Sloan and Koh, 2008). But it is hard to quantitatively evaluate the inhibiting effect of salt on the BSR depth due to the difficulty associated with predicting the salinity increased by upward movement of dissolved salt via diffusion and advection. Uncertainties in the modelled BSR depths may also stem from error estimates of geothermal gradient, thermal conductivity of sediments, velocity model in the subsurface and temperatures at the seabed. It cannot be entirely ruled out that the match between the modelled and observed BSR is a coincidence resulting from these uncertainties.

7.2 Implications

In general, hydrated sediment is an effective barrier for free gas during its ascent in the subsurface (Nimblett and Ruppel, 2003). Occasionally this gas can reach the seabed by itself, such as when the pore pressure of its reservoir in a hydrate province reaches a level that the fault slip can occur (Hornbach et al., 2004). But the height of gas column in this case is significantly lower than the critical height recorded in the Blake Ridge (~150 – 290 m, Hornbach et al., 2004). Given that the trap created by the BSR relocation is fully charged, the height of the gas column of the formed gas accumulation is estimated to be no more than 50 ms (c. 45 m). This suggests that the capillary entry pressure of overburden sediment along

fault is lower than that of the unfaulted sediment and this offers permeable route for gas to reach the seabed.

Gas-rich pore fluids are interpreted to reach the seabed along the faults in this study, rather than migrating as a three-phase flow-controlled process to rise the gas-hydrate front (Liu and Flemings, 2006) or along the fractures triggered by overpressured gas (Flemings et al., 2003). The morphological features along the fault scarps at the seabed represent multiple gas vents at the sites, which together constitute a venting system allowing methane to bypass the feather edge of marine hydrate. During the ascent of methane in the HSZ, porous and permeable sediments could capture part of this methane, such as the case of the PHAAs, preventing or slowing down the transport of methane towards the seabed. This can also be achieved by the reformation of hydrates along the faults (Ahn et al., 2012), which can clog the pores of the sediments within faults and hence lower the permeability. However, methane could still reach the seabed due to the water-free, hypersaline or warmer pore environment during the ascent of methane via advection (Wood et al., 2002; Tréhu et al., 2004; Liu and Flemings, 2006). Given that methane re-capturing and hydrate reforming could not prevent methane from approaching the seabed, we think that methane was intermittently released into the ocean due to the episodicity of gas migration along the pre-existing faults (Tryon et al., 1999).

A BSR is present over the study area but mostly absent landward of it (Fig. 6a-c). This is different from the area (marked in yellow box, Fig. 1a) to the north where sedimentary context is similar but the BSR can be commonly observed (Davies et al., 2015). An explanation for its absence landward is that methane venting above the diapir prevents landward gas migration (Fig. 6d). Absence of free gas near the landward limit of the feather

edge implies less methane locked-up in marine hydrates will be susceptible to being released in a warmer ocean in the future. Therefore, diapirism can increase methane emission into the ocean before it gets warmer and melts the marine hydrate hosted in the sub-seabed sediment. The bottom water temperature fluctuated seasonally by $< 1^{\circ}\text{C}$ offshore of Mauritania after the year 2000 (data from WOD) and this can destabilise the gas hydrates locating at $< \sim 20$ mbsf near the landward limit of the feather edge (we used the 2-D heat diffusion model of Li et al (2017) to see where gas hydrates was stable after the year 2000, not shown here). Due to the gas vent intercepting lateral gas migration, we predict that there are few gas hydrates near the landward limit of the feather edge in the study area and hence no significant amount of methane have been released from the seabed at the site since the year 2000 (acquisition time of the seismic dataset is between November 1999 and March 2000, Colman et al., 2005).

8 Conclusions

3-D seismic data provide compelling evidence for the occurrence of a gas venting system, offshore Mauritania. A salt diapir provides the conditions to create migration pathways for focused fluid of free gas that bypasses the feather edge of marine hydrate. The gas venting system inhibits gas migration landward into the shallow feather edge region. This reduces the volume of methane that would be susceptible to the short-term oceanic warming after the year 2000 and a probably warmer world in the future.

Acknowledgments

We thank Durham University and China Scholarship Council for supporting this research. We are grateful to Tullow Oil and Petronas for the permission to release this seismic survey offshore Mauritania. We also thank Dave Stevenson and Gary Wilkinson for

maintaining the IT facilities in Earth Imaging Laboratory (EIL) and the Landmark University Grant Program for providing the DecisionSpace suite.

References

- Abrams, M.A., 1992, Geophysical and geochemical evidence for subsurface hydrocarbon leakage in the Bering Sea, Alaska. *Mar. Pet. Geol.* **9**(2), 208-221.
- Ahn, T., Park, C., Lee, J., Kang, J.M., and Nguyen, H.T., 2012, Experimental characterization of production behaviour accompanying the hydrate reformation in methane-hydrate-bearing sediments. *J. Can. Pet. Technol.* **51**(01), 14-19.
- Anderson, A.L., and Hampton, L.D., 1980, Acoustics of gas-bearing sediments I. Background. *J. Acoust. Soc. Am.* **67**(6), 1865-1889.
- Archer, D., Buffett, B., and Brovkin, V., 2009, Ocean methane hydrates as a slow tipping point in the global carbon cycle. *Proc. Natl. Acad. Sci.* **106**(49), 20596-20601.
- Bangs, N.L., Musgrave, R.J., and Tréhu, A.M., 2005, Upward shifts in the southern Hydrate Ridge gas hydrate stability zone following postglacial warming, offshore Oregon. *J. Geophys. Res.:Solid Earth* **110**(B3).
- Berndt, C., Feseker, T., Treude, T., Krastel, S., Liebetrau, V., Niemann, H., Bertics, V.J., Dumke, I., Dünnebier, K., Ferré, B. and Graves, C., 2014, Temporal constraints on hydrate-controlled methane seepage off Svalbard. *Science* **343**(6168), 284-287.
- Biajoch, A., Treude, T., Rüpke, L.H., Riebesell, U., Roth, C., Burwicz, E.B., Park, W., Latif, M., Böning, C.W., Madec, G., and Wallmann, K., 2011, Rising Arctic Ocean temperatures cause gas hydrate destabilization and ocean acidification, *Geophys. Res. Lett.* **38**(8).
- Brown, A., 2010, Interpretation of Three-dimensional Seismic Data, seventh ed. Tulsa.

- Cartwright, J., Huuse, M., and Aplin, A., 2007, Seal bypass system. *Am. Assoc. Pet. Geol.* **91**(8), 1141-1166.
- Cartwright, J., and Santamarina, C., 2015, Seismic characteristics of fluid escape pipes in sedimentary basins: Implications for pipe genesis. *Mar. Pet. Geol.* **65**, 126-140.
- Catterall, V., Redfern, J., Gawthorpe, R., Hansen, D., and Thomas, M., 2010, Architectural style and quantification of a submarine channel–levee system located in a structurally complex area: offshore Nile Delta. *J. Sediment. Res.* **80**(11), 991-1017.
- Colman, J., Gordon, D., Lane, A., Forde, M., and Fitzpatrick, J., 2005, Carbonate mounds off Mauritania, Northwest Africa: status of deep-water corals and implications for management of fishing and oil exploration activities. *Cold-water corals and ecosystems*, 417-441.
- Crutchley, G.J., Klaeschen, D., Planert, L., Bialas, J., Berndt, C., Papenberg, C., Hensen, C., Hornbach, M.J., Krastel, S., and Brueckmann, W., 2014, The impact of fluid advection on gas hydrate stability. Investigations at sites of methane seepage offshore Costa Rica. *Earth Planet. Sci. Lett.* **401**, 95-109.
- Davies, R.J., and Clarke, A.L., 2010, Methane recycling between hydrate and critically pressured stratigraphic traps, offshore Mauritania. *Geology* **38**(11), 963-966.
- Davies, R.J., Thatcher, K.E., Armstrong, H., Yang, J.X., and Hunter, S., 2012, Tracking the relict bases of marine methane hydrates using their intersections with stratigraphic reflections. *Geology* **40**(11), 1011-1014.
- Davies, R.J., Thatcher, K.E., Mathias, S.A., and Yang, J., 2012, Deepwater canyons: An escape route for methane sealed by methane hydrate. *Earth Planet. Sci. Lett.* **323**, 72-78.
- Davies, R.J., Yang, J., Li, A., Mathias, S., and Hobbs, R., 2015, An irregular feather-edge and potential outcrop of marine gas hydrate along the Mauritanian margin. *Earth Planet.*

Sci. Lett. **423**, 202-209.

- Dickens, G.R., 2003, Rethinking the global carbon cycle with a large, dynamic and microbially mediated gas hydrate capacitor, *Earth Planet. Sci. Lett.* **213**(3), 169-183.
- Dimitrov, L.I., 2002, Mud volcanoes—the most important pathway for degassing deeply buried sediments. *Earth-Sci. Rev.* **59**(1), 49-76.
- Flemings, P.B., Liu, X., and Winters, W.J., 2003, Critical pressure and multiphase flow in Blake Ridge gas hydrates. *Geology* **31**(12), 1057-1060.
- Helgerud, M.B., Waite, W.F., Kirby, S.H., and Nur, A., 2009, Elastic wave speeds and moduli in polycrystalline ice Ih, sI methane hydrate, and sII methane-ethane hydrate *J. Geophys. Res.:Solid Earth* **114**(B2).
- Henrich, R., Hanebuth, T.J.J., Krastel, S., Neubert, N., and Wynn, R.B., 2008, Architecture and sediment dynamics of the Mauritania Slide Complex. *Mar. Pet. Geol.* **25**(1), 17-33.
- Henrich, R., Cherubini, Y., and Meggers, H., 2010, Climate and sea level induced turbidite activity in a canyon system offshore the hyperarid Western Sahara (Mauritania): The Timiris Canyon. *Mar. Geol.* **275**(1-4), 178-198.
- Hornbach, M.J., Ruppel, C., Saffer, D.M., Van Dover, C.L., and Holbrook, W. S., 2005, Coupled geophysical constraints on heat flow and fluid flux at a salt diapir. *Geophys. Res. Lett.* **32**(24).
- Hornbach, M.J., Saffer, D.M., and Holbrook, W.S., 2004, Critically pressured free-gas reservoirs below gas-hydrate provinces. *Nature* **427**(6970), 142-144.
- Hovland, M., and Judd, A.G., 1988, Seabed pockmarks and seepages: impact on geology, biology and the marine environment.
- Hovland, M., and Svensen, H., 2006, Submarine pingoes: Indicators of shallow gas hydrates in a pockmark at Nyegga, Norwegian Sea. *Mar. Geol.* **228**(1), 15-23.

- Judd, A.G., 2003. The global importance and context of methane escape from the seabed. *Geo-Marine Letters* **23**(3-4), 147-154.
- Krastel, S., Wynn, R.B., Hanebuth, T.J.J., Henrich, R., Holz, C., Meggers, H., Kuhlmann, H., Georgiopoulou, A., and Schulz, H.D., 2006, Mapping of seabed morphology and shallow Sediment structure of the Mauritania continental margin, Northwest Africa: some implications for geohazard potential. *Nor. J. Geol.* **86**(3), 163-176.
- Kvenvolden, K.A., 1993, Gas Hydrates - Geological Perspective and Global Change. *Rev. Geophys.* **31**(2), 173-187.
- Li, A., Davies, R.J. and Yang, J., 2016. Gas trapped below hydrate as a primer for submarine slope failures. *Mar. Geol.* **380**, 264-271.
- Li, A., Davies, R.J., and Mathias, S., 2017. Methane hydrate recycling offshore of Mauritania probably after the last glacial maximum. *Mar. Pet. Geol.* in press.
- Liu, X., and Flemings, P.B., 2006, Passing gas through the hydrate stability zone at southern Hydrate Ridge, offshore Oregon, *Earth Planet. Sci. Lett.* **241**(1), 211-226.
- Lu, Z., and Sultan, N., 2008, Empirical expressions for gas hydrate stability law, its volume fraction and mass-density at temperatures 273.15 K to 290.15 K, *Geochem. J.* **42**(2), 163-175.
- Mackay, J.R., 1987, Some mechanical aspects of pingo growth and failure, western Arctic coast, Canada. *Can. J. Earth Sci.* **24**(6), 1108-1119.
- MacKay, M.E., Jarrard, R.D., Westbrook, G.K., and Hyndman, R.D., 1994, Origin of bottom-simulating reflectors: geophysical evidence from the Cascadia accretionary prism. *Geology* **22**(5), 459-462.
- Marín-Moreno, H., Minshull, T.A., Westbrook, G.K., Sinha, B., and Sarkar, S., 2013, The response of methane hydrate beneath the seabed offshore Svalbard to ocean warming during the next three centuries. *Geophys. Res. Lett.* **40**(19), 5159-5163.

- McGinnis, D.F., Greinert, J., Artemov, Y., Beaubien, S.E. and Wüest, A.N.D.A., 2006, Fate of rising methane bubbles in stratified waters: How much methane reaches the atmosphere?, *J. Geophys. Res.: Oceans* **111**(C9).
- Milkov, A.V., 2000. Worldwide distribution of submarine mud volcanoes and associated gas hydrates. *Mar. Geol.* **167**(1), 29-42.
- Moss, J.L., and Cartwright, J., 2010, 3-D seismic expression of km-scale fluid escape pipes from offshore Namibia. *Basin Res.* **22**(4), 481-501.
- Nimblett, J., and C. Ruppel, 2003, Permeability evolution during the formation of gas hydrates in marine sediments, *J. Geophys. Res.* **108**(B9), 2420.
- Phrampus, B.J., and Hornbach, M.J., 2012, Recent changes to the Gulf Stream causing widespread gas hydrate destabilization. *Nature* **490**(7421), 527-530.
- Rad, U., Hinz, K., Sarnthein, M., and Seibold, E., 1982, Geology of the Northwest African continental margin. Springer-Verlag Berlin Heidelberg, 160-181.
- Roberts, H.H., 2001, Fluid and Gas Expulsion on the Northern Gulf of Mexico Continental Slope: Mud-Prone to Mineral-Prone Responses. Natural gas hydrates: occurrence, distribution, and detection, 145-161.
- Roberts, H.H., Hardage, B.A., Shedd, W.W., and Hunt Jr, J., 2006, Seafloor reflectivity—an important seismic property for interpreting fluid/gas expulsion geology and the presence of gas hydrate. *The Leading Edge* **25**(5), 620-628.
- Ruppel, C.D., 2011. Methane hydrates and contemporary climate change. *Nature Education Knowledge* **3**(10), 29.
- Schmuck, E.A., and Paull, C.K., 1993, Evidence for gas accumulation associated with diapirism and gas hydrates at the head of the Cape Fear Slide. *Geo-Mar. Lett.* **13**(3), 145-152.
- Serié, C., Huuse, M., and Schødt, N.H., 2012, Gas hydrate pingoes: Deep seafloor evidence

- of focused fluid flow on continental margins. *Geology* **40**(3), 207-210.
- Shipley, T.H., Houston, M.H., Buffler, R.T., Shaub, F.J., McMillen, K.J., Ladd, J.W., and Worzel, J.L., 1979, Seismic evidence for widespread possible gas hydrate horizons on continental slopes and rises. *AAPG Bull.* **63**(12), 2204-2213.
- Skarke, A., Ruppel, C., Kodis, M., Brothers, D., and Lobecker, E., 2014, Widespread methane leakage from the sea floor on the northern US Atlantic margin, *Nat. Geosci.* **7**(9), 657-661.
- Sloan, E.D., and Koh, C.A., 2008, Clathrate Hydrates of Natural Gases, third ed., Boca Raton: CRC Press.
- Soloviev, V., and Ginsburg, G.D., 1994, Formation of submarine gas hydrates. *Bull. Geol. Soc. Denmark* **41**, 86-94.
- Somoza, L., Leon, R., Ivanov, M., Fernández-Puga, M.C., Gardner, J.M., Hernández-Molina, F.J., Pinheiro, L.M., Rodero, J., Lobato, A., Maestro, A., and Vázquez, J.T., 2003, Seabed morphology and hydrocarbon seepage in the Gulf of Cadiz mud volcano area: Acoustic imagery, multibeam and ultra-high resolution seismic data. *Mar. Geol.* **195**(1), 153-176.
- Tréhu, A.M., Flemings, P.B., Bangs, N.L., Chevallier, J., Gracia, E., Johnson, J.E., Liu, C.-S., Liu, X., Riedel, M., and Torres, M.E., 2004, Feeding methane vents and gas hydrate deposits at south Hydrate Ridge, *Geophys. Res. Lett.* **31**(23).
- Tryon, M.D., Brown, K.M., Torres, M.E., Tréhu, A.M., McManus, J., and Collier, R.W., 1999, Measurements of transience and downward fluid flow near episodic methane gas vents, Hydrate Ridge, Cascadia. *Geology* **27**(12), 1075-1078.
- Vear, A., 2005. Deep-water plays of the Mauritanian continental margin. Petroleum Geology Conference Series **6**, 1217–1232.

- Westbrook, G.K., Thatcher, K.E., Rohling, E.J., Piotrowski, A.M., Pälike, H., Osborne, A.H., Nisbet, E.G., Minshull, T.A., Lanoisellé, M., James, R.H., and Hühnerbach, V., 2009, Escape of methane gas from the seabed along the West Spitsbergen continental margin. *Geophys. Res. Lett.* **36**(15).
- Wood, W.T., Gettrust, J.F., Chapman, N.R., Spence, G. D., and Hyndman, R. D., 2002, Decreased stability of methane hydrates in marine sediments owing to phase-boundary roughness, *Nature* **420**(6916), 656-660.
- Yang, J., and Davies, R.J., 2013, Gravity-driven faults: migration pathways for recycling gas after the dissociation of marine gas hydrates. *Mar. Geol.* **336**, 1-9.
- Zhang, Z., McConnell, D.R. and Han, D.H., 2012, Rock physics-based seismic trace analysis of unconsolidated sediments containing gas hydrate and free gas in Green Canyon 955, Northern Gulf of Mexico. *Mar. Pet. Geol.* **34**(1), 119-133.
- Zühlsdorff, C., Wien, K., Stuut, J.B., and Henrich, R., 2007, Late Quaternary sedimentation within a submarine channel–levee system offshore Cap Timiris, Mauritania. *Mar. Geol.* **240**(1), 217-234.

Figure captions

Fig.1 (a) Extent of the area covered by the 3-D seismic survey and the location of the study area. The blue box of solid lines marks where the relatively complete feather edge was described by Davies et al. (2015). (b) Dip-magnitude map of the seabed in the study area showing the fault scarp and some reliefs (named as I, II, III and IV). FS – fault scarp. There are some linear features caused by acquisition noise and they are parallel to the inline direction. (c) 3-D imaging of the faults (named as F1–13) from top view. The white arrows mark the displacement direction of the hanging wall. Please note not all the faults terminate at

the seabed. (d) A representative seismic cross section showing the pattern of the faults and their spatial relationship between the underlying salt diapir.

Fig.2 (a–b) Representative seismic cross sections displaying the spatial relationship between the reliefs at the seabed, the faults and the salt diapir. The acoustic wipe-out (AWO) shows up below I-IV and in the zone bounded by F1, F2 and F4. (c–f) Zoom-in figures showing the cross-sectional geometry of I-IV. (g–j) 3-D imaging of the bathymetry exhibiting the morphology of I-IV.

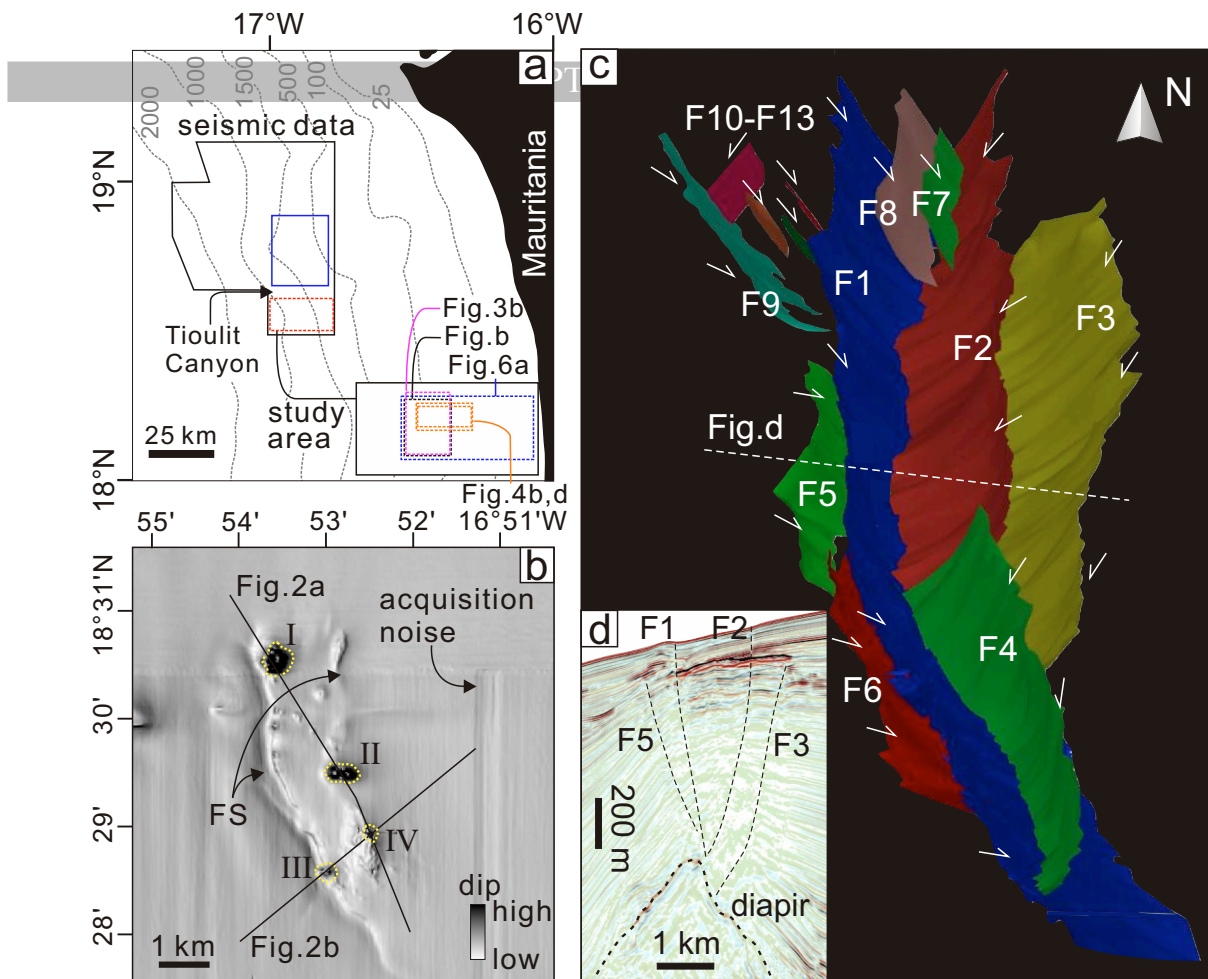
Fig.3 (a) A seismic cross section showing the upwarping section of the BSR. A different colour scheme is used to highlight its polarity (cyan-yellow loop) that is opposite to that of the seabed reflection (yellow-cyan loop). A flat spot is found under the upwarping BSR. Please note that this figure is exaggerated vertically. HA – high amplitude, LA – low amplitude in this and subsequent figures. (b) RMS amplitude map of the BSR. The white dashed and solid lines are the contours of the vertical distance (measured in ms, TWTT) between the BSR and surface a. Surface a is an assumed surface and on each cross line (E-W oriented) it is a segment defined by the down-dip (1, marked in inset) and the up-dip point (2) along the BSR. The yellow dashed lines mark the outline of a buried old canyon and it is described in section 6.3.

Fig.4 (a) Seismic cross section displaying the vertical stacking pattern of the multistory channel-levee systems. Reflection A, which is interpreted as the levee sediment hosting hydrates, downlaps upon a paleo-seabed B. (b) Map showing the depth of the paleo-seabed B. The place in where the old channel diverges is not clearly shown by the seismic dataset. (c) A seismic cross section showing the spatial relationship between the BSR and the reflection A.

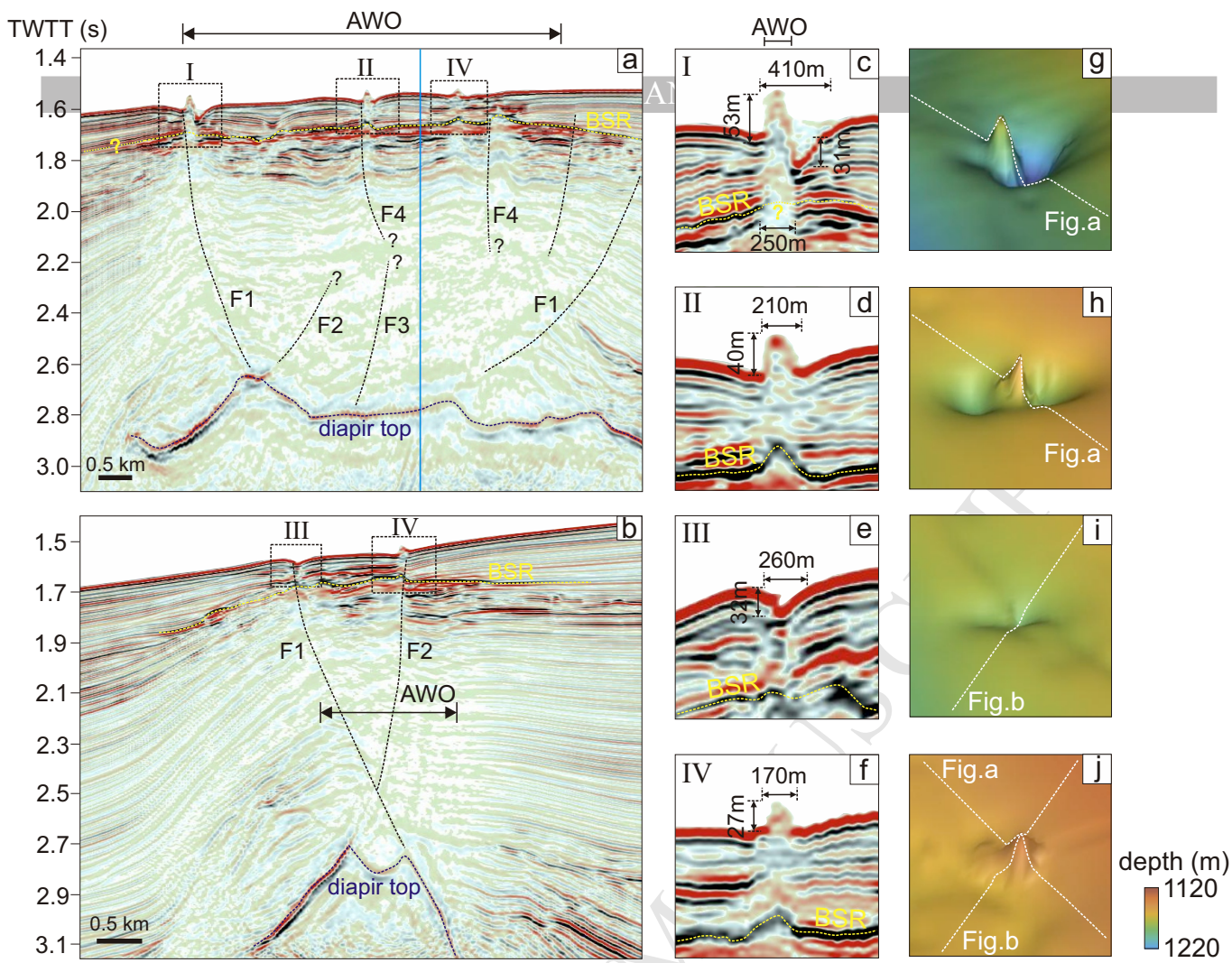
(d) RMS amplitude map of the reflection A. Some positive high amplitude anomalies (PHAAs) show up at both sides of the buried canyon.

Fig.5 Modelling result of 2-D heat conduction. The black dashed line marks the top of the diapir. The blue numbers indicate the temperature of each isothermal line. The black arrows mark the places where there are some minor discrepancies between the modelled BSR and the observation result.

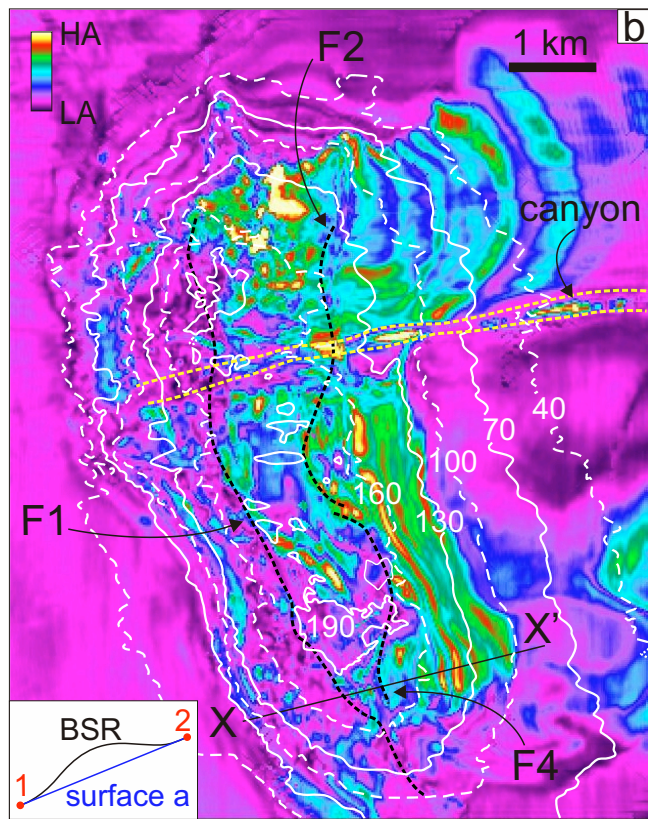
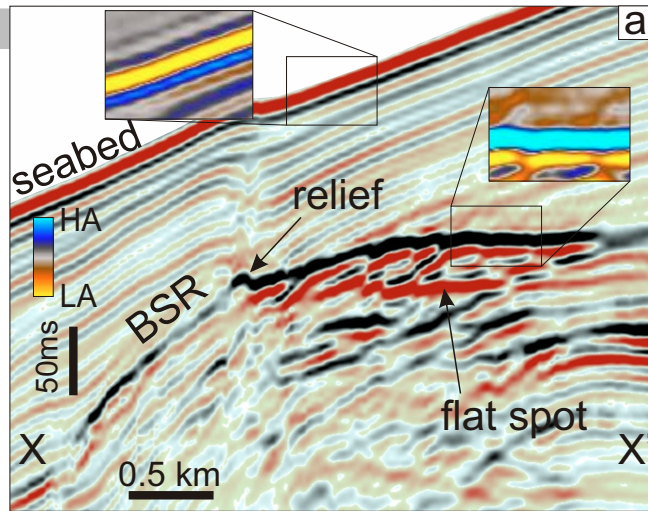
Fig.6 (a) The BSR depth measured in two-way travel time (TWTT). No-data places (black colour) indicate where the BSR cannot be observed in the seismic cross section. (b, c) Two representative seismic sections showing that BSR can be tracked above the studied diapir, but is absent elsewhere except the region to the southeast of it. (d) Schematic diagram showing gas migration and where the BSR is present. Black arrows mark the displacement direction of the hanging wall. The dimension of the diapir and the levee is not to scale. PM – pockmark, M – mound, GC – gas concentration, HC – hydrate concentration, GM – gas migration.



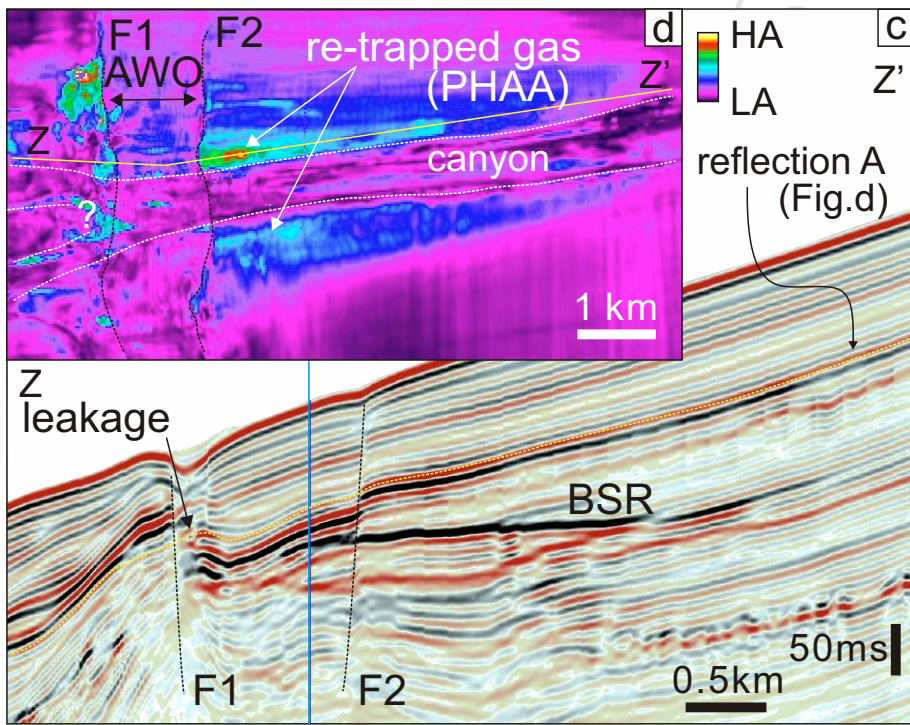
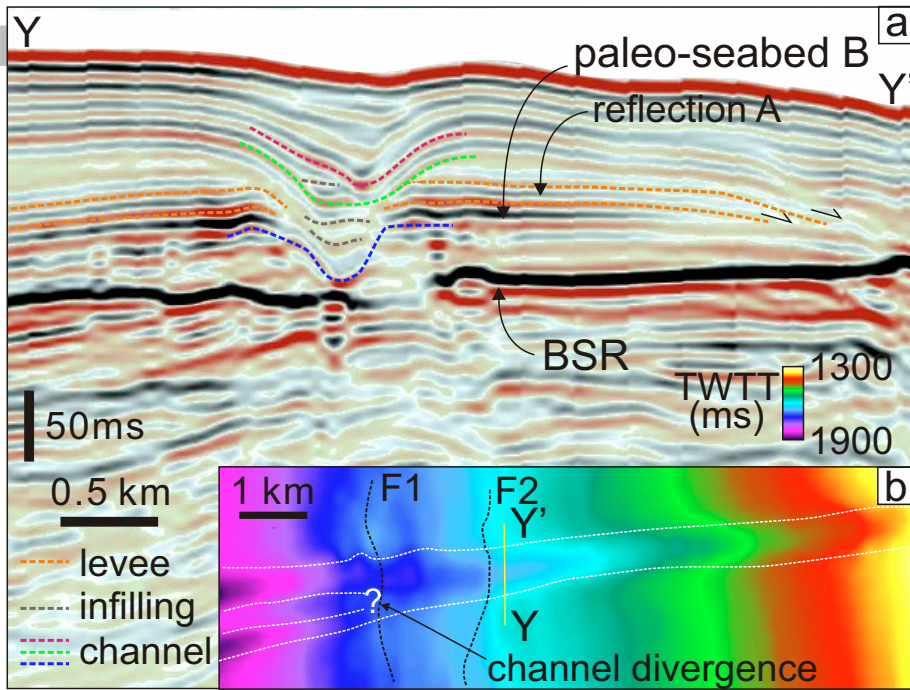
ACCEPTED MANUSCRIPT

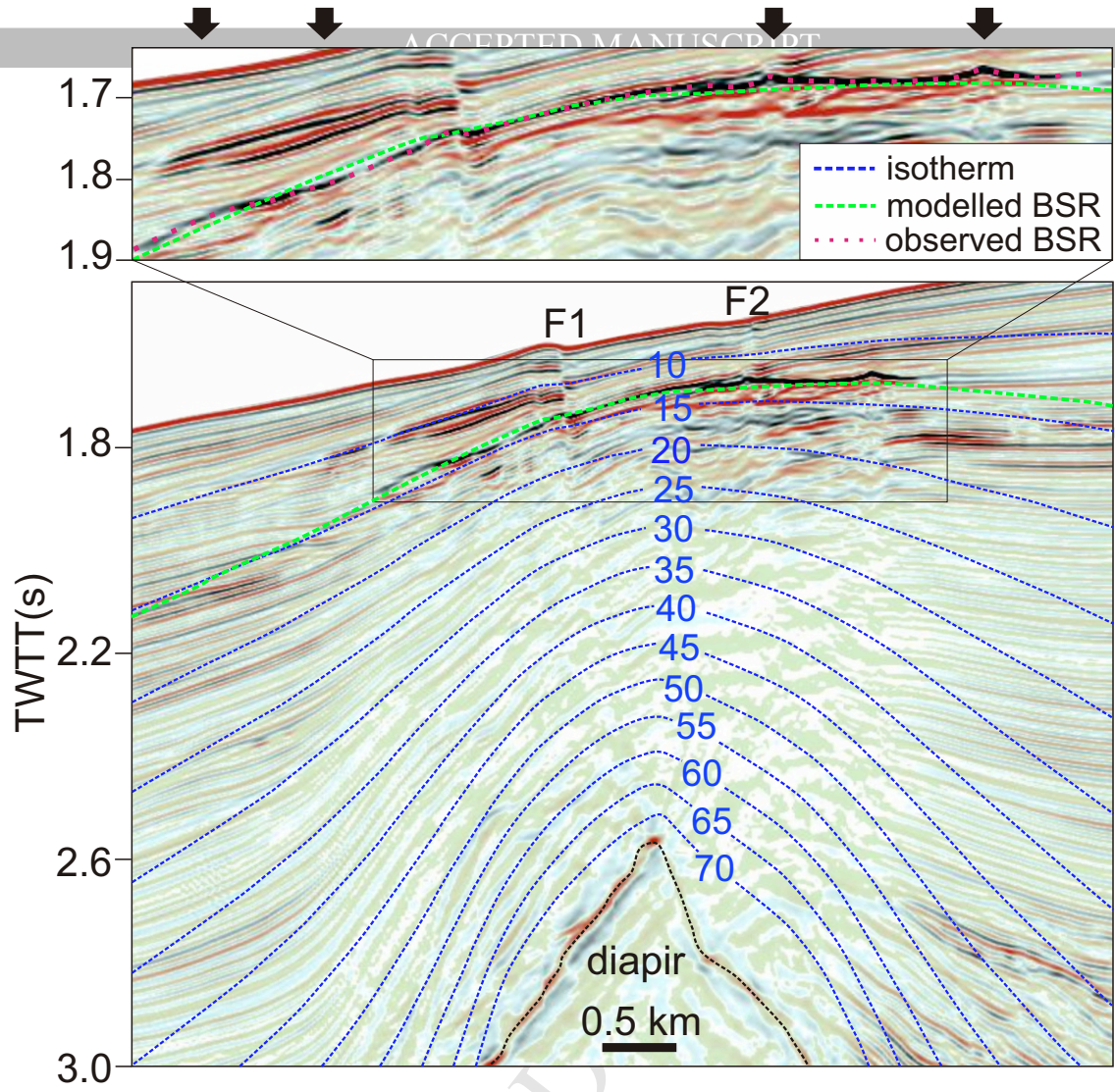


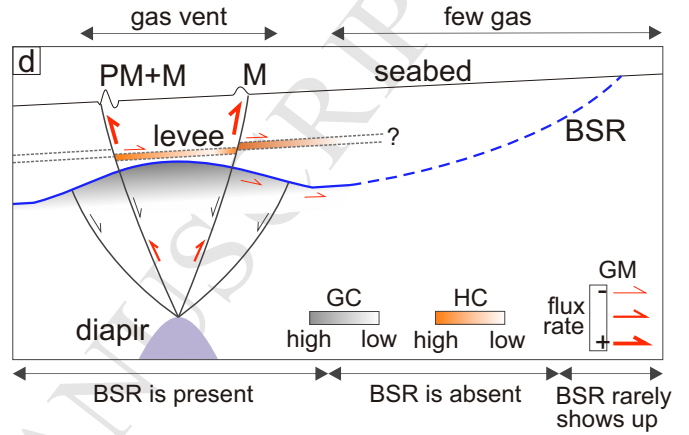
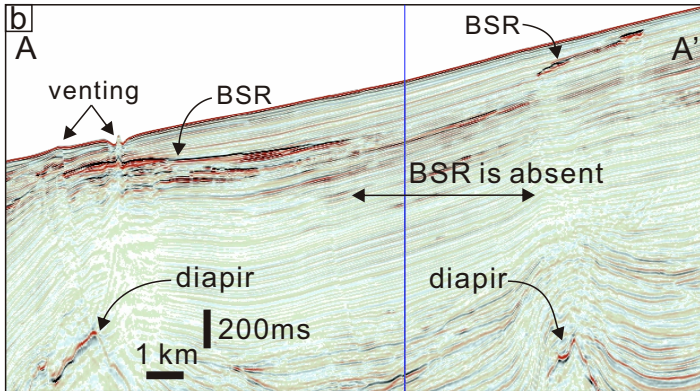
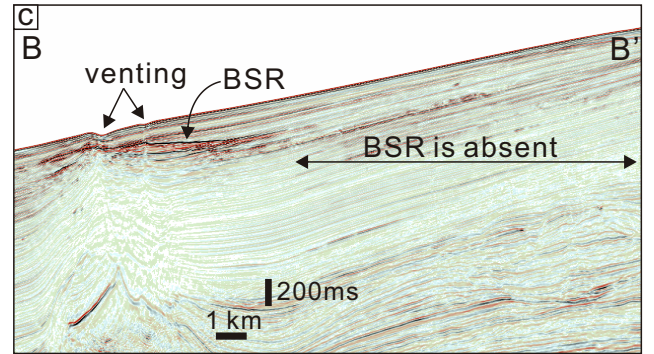
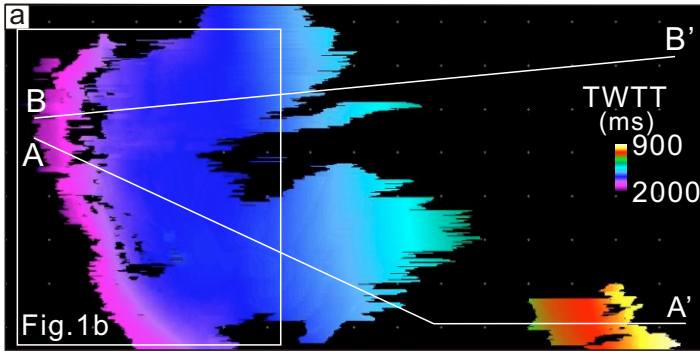
ACCEPTED



BSR upwarping







Highlights:

A gas venting system is imaged using 3-D seismic data offshore Mauritania.

Free gas bypassed the HSZ and migrated along the faults to reach the seabed.

The local BSR shoaling is caused by more heat conduction of a salt diapir.

Massive warming-induced methane seafloor release is unlikely since the year 2000.

ACCEPTED MANUSCRIPT